J. Fluid Mech. (2014), *vol.* 755, *pp.* 628–653. © Cambridge University Press 2014
doi:10.1017/jfm.2014.432

Inertially induced cyclic solutions in thin-film free-surface flows

C. M. Groh[1,2] **and M. A. Kelmanson**[1,†]

[1]Department of Applied Mathematics, University of Leeds, Leeds LS2 9JT, UK

[2]Department of Radiation Oncology, University of Würzburg, D-97080 Würzburg, Germany

(Received 22 November 2013; revised 7 July 2014; accepted 22 July 2014;
first published online 22 August 2014)

New mechanisms are discovered regarding the effects of inertia in the transient Moffatt–Pukhnachov problem (*J. Méc.*, vol. 187, 1977, pp. 651–673) on the evolution of the free surface of a viscous film coating the exterior of a rotating horizontal cylinder. Assuming two-dimensional evolution of the film thickness (i.e. neglecting variation in the axial direction), a multiple-timescale procedure is used to obtain explicitly parameterized high-order asymptotic approximations of solutions of the spatio-temporal evolution equation. Novel, hitherto-unexplained transitions from stability to instability are observed as inertia is increased. In particular, a critical Reynolds number Re_c is predicted at which occurs a supercritical pitchfork bifurcation in wave amplitude that is fully explained by the new asymptotic theory. For $Re < Re_c$, free-surface profiles converge algebraically-cum-exponentially to a steady state and, for $Re > Re_c$, stable temporally periodic solutions with leading-order amplitudes proportional to $(Re - Re_c)^{1/2}$ are found, i.e. in the régime in which previous related literature predicts exponentially divergent instability. For $Re = Re_c$, stable solutions are found that decay algebraically to a steady state. A model solution is proposed that not only captures qualitatively the interaction between fundamental and higher-order wave modes but also offers an explanation for the formation of the lobes observed in Moffatt's original experiments. All asymptotic theory is convincingly corroborated by numerical integrations that are spectrally accurate in space and eighth/ninth-order accurate in time.

Key words: lubrication theory, parametric instability, thin films

1. Introduction

Although the influences of gravitational and capillary effects on the stability of coating and rimming flows have been the subject of numerous asymptotic and numerical studies, the explicit influence of inertia has been less widely considered, e.g. as in Hosoi & Mahadevan (1999), Benilov & O'Brien (2005), Noakes, King & Riley (2006), Kelmanson (2009*b*), Pougatch & Frigaard (2011) and Benilov & Lapin (2013). As a result, there remain unresolved questions about both the qualitative and quantitative influences of inertia on the mechanisms describing the transition between stable and unstable flow régimes and, in particular, about the flow evolution

† Email address for correspondence: mark@maths.leeds.ac.uk

https://doi.org/10.1017/jfm.2014.432 Published online by Cambridge University Press

in the latter. Whilst the present results – and those in a plethora of related theoretical studies – are derived from analyses of two-dimensional coating/rimming models that neglect axial effects, it is well known that the experiments of, e.g. Moffatt (1977) and Hynes (1978) reveal an onset of instability that results in the development of three-dimensional axially-and-azimuthally isolated 'lobe-like' profiles. This naturally invites the question of the extent to which two-dimensional analyses are physically realistic. However, there is to date – see, e.g., the three-dimensional studies of Hosoi & Mahadevan (1999), Pougatch & Frigaard (2011) and Benilov & Lapin (2013) – neither a computational nor theoretical conclusive answer to the question, which is revisited at the end of § 5, of the exact nature of the axial–azimuthal interaction that induces three-dimensional instability. With this in mind, it is hoped that the accurate numerical and theoretical approaches presented herein – which yield (see § 5.3) large-time azimuthally isolated lobe-like profiles similar to those observed in the above-cited experiments – will initiate further studies that are able to incorporate appropriate axial effects in order to resolve this important question.

Interpreting the influence of inertia is a subtle matter that has invited contradicting conclusions drawn from thin-film approximations obtained via different scalings: for example, the asymptotic analysis of Kelmanson (2009*b*) resolves apparent conflicts between predictions in Benilov & O'Brien (2005) and Noakes *et al.* (2006), which respectively conclude that inertial effects destabilize and stabilize rimming flows. Specifically, Kelmanson (2009*b*) reveals that the different scalings inherent in the two prior studies yield results that should not be compared because their underlying asymptotics are not uniformly valid in the same parameter régime. Pougatch & Frigaard (2011) implicitly corroborate this observation through numerically obtained growth rates determined via a linearized stability analysis; they conclude that 'inertia may stabilize or destabilize the flow depending on the values of other parameters'.

The qualitative consequences of different scalings are investigated in Kelmanson (2009*b*) via an explicit reconstruction and comparison of the asymptotic coating/rimming-flow analyses of Benjamin, Pritchard & Tavener (1993), Ashmore, Hosoi & Stone (2003) and Benilov & O'Brien (2005). The comparison reveals a scaling-dependent promotion and demotion – respectively, into dominant and sub-dominant positions in the asymptotically ordered hierarchy whose leading-order component is the spatio-temporal evolution equation for the film thickness – of two different types of inertial contributions, christened in Kelmanson (2009*b*) as 'pure-inertial' and 'mixed-gravitational inertial'. That is, the promotion and demotion of inertial terms in the thin-film evolution equation is dictated by the *a priori* rescaling of all physical and geometric parameters.

Much previous work on two- and three-dimensional coating and rimming flows considers stability via the numerical computation of the relationship between wavenumbers and growth rates (e.g. Benilov & O'Brien 2005; Pougatch & Frigaard 2011; Benilov & Lapin 2013); occasionally (e.g. Hosoi & Mahadevan 1999; Evans, Schwarz & Roy 2004, 2005), finite-time free-surface profiles are numerically computed. By their nature, such numerical studies cannot yield qualitative information regarding spatio-temporal, finite-time coating/rimming-flow dynamics. However, the use of algebraic manipulators has enabled the development and implementation of increasingly powerful automated multiple-timescale asymptotic methods (Hinch & Kelmanson 2003; Hinch, Kelmanson & Metcalfe 2004; Groh & Kelmanson 2009, 2012; Kelmanson 2009*a*,*b*), in the penultimate of which all results are validated against spectrally accurate *transient* numerical methods (cf. the exponentially convergent collocation method used by Karabut (2007) and Pougatch & Frigaard

https://doi.org/10.1017/jfm.2014.432 Published online by Cambridge University Press

(2011) on steady-state problems). Through such asymptotic studies, many qualitative and quantitative results have been found relating to the temporal dynamics of coating flow, and the present study is conducted in the spirit of these papers, of which Kelmanson (2009*b*) forms the primary motivation.

In Kelmanson (2009*b*), explicit formulae obtained via two-timescale asymptotics are validated against extrapolated finite-difference numerical results. It is found therein that inertia destabilizes coating flow (in agreement with Noakes *et al.* 2006) when the Reynolds number Re exceeds a critical threshold, Re_c say, for which an explicit formula is obtained. For $Re < Re_c$, the asymptotic solution is exponentially convergent to a stable steady state; for $Re > Re_c$, the solution diverges exponentially; for $Re = Re_c$, cyclic – i.e. temporally periodic and bounded – solutions are discovered that neither decay nor become unstable. That is, the two-timescale asymptotics of Kelmanson (2009*b*) predict the existence of cyclic solutions at only the critical value $Re = Re_c$. Clearly, such a unique neutral stability will be predicted by any linearized stability analysis that assumes a pure-exponential perturbation from the steady state.

By contrast, using a spectrally accurate computational technique developed and validated in Groh & Kelmanson (2009, 2012), new numerical integrations (discussed in § 2.2) of the thin-film evolution equation derived in Kelmanson (2009*b*) presently reveal the existence of cyclic solutions for a range $Re > Re_c$, in which both the linearized stability analysis and the two-timescale asymptotics predict full-blown instability. As demonstrated in this paper, the transient perturbation is in fact not purely exponential, as assumed in all previous stability analyses, and it transpires that asymptotics using more than two timescales are required to determine the correct – in the sense of quantitative agreement with computations – form of transient perturbation. Specifically, by using the highly flexible 'm-timescale' asymptotics developed and validated in Groh & Kelmanson (2012), explicit formulae are presently obtained for a newly discovered algebraic-cum-exponential transient perturbation that yields results that are in excellent agreement with those of validating spectrally accurate numerics.

The remainder of this paper is structured as follows. Section 2.1 contains a coating-flow problem formulation that presents only those aspects that are relevant and distinctive to the present consideration of inertial effects; full derivations and asymptotic arguments underpinning thin-film evolution equations for coating/rimming flows are given in almost all of the above-cited literature. A discussion is undertaken of the competing physical influences of capillarity, gravity, hydrostatic pressure and inertia, including a motivation for the scalings used. With the theoretical framework established, intermediate numerical computations are performed in § 2.2 in order to motivate the remainder of the study. In § 3.1, an explicit (asymptotic) steady-state solution is derived to quantify the effects of inertia, and a simple yet apparently new physical explanation of its destabilizing effect on the steady state is presented. This is followed in § 3.2 by a linearized analysis, about the asymptotic steady-state solution, in order to gain an insight into the stability properties of the thin-film steady-state profile with respect to infinitesimally small disturbances. A more complete insight into the finite-time transient behaviour of the free-surface evolution is gained in § 4, where the inertial evolution equation of Kelmanson (2009*b*) is studied by using seven timescales in the m-timescale method of Groh & Kelmanson (2012). In particular, the stable and unstable régimes of the solution are classified and the transition between these régimes is discussed. The predicted class of unstable solutions is corroborated by spectral numerics, with which the asymptotic predictions are found to be in excellent agreement. The results in § 5 fall naturally into three distinct subsections. In § 5.1, a qualitative validation of the asymptotics is undertaken in terms of physical

https://doi.org/10.1017/jfm.2014.432 Published online by Cambridge University Press

effects. In § 5.2, a quantitative validation is conducted, and all asymptotic results are demonstrated to be in excellent agreement with those of spectrally accurate numerical computations. Additionally, convincing evidence is provided that higher-order physical effects such as hydrostatic pressure and mixed gravitational–inertial terms can be ignored in the modelling of this and related problems. A detailed investigation of the nature of the transition from asymptotically stable to cyclic solutions is made in § 5.3, in which leading-order asymptotics reveal that the fundamental wave mode, the only one surviving to large times, undergoes a supercritical pitchfork bifurcation at the critical Reynolds number $Re = Re_c$, the amplitude thereafter growing as $(Re - Re_c)^{1/2}$. Section 6 concludes with an investigation of higher-mode instability in an attempt to explain modal interactions observed in spectral numerical solutions. A model form of solution is proposed that not only captures well the qualitative behaviour of the numerics but also proposes (for future work) how asymptotic methods might be developed to model the higher-mode interactions in a more accurate quantitative fashion.

2. Thin-film evolution equation

2.1. *Formulation*

The evolution of a two-dimensional azimuthal section of a viscous capillary film coating the exterior of a horizontal rotating cylinder is analysed in standard cylindrical-polar coordinates (r, θ) centred on the axis of the cylinder, which has radius a and rotates about its horizontal axis with constant angular velocity Ω. The coating film, of thickness $h(\theta, t)$ at station θ and time t, comprises homogeneous fluid of dynamic viscosity, density and surface tension μ, ρ and σ respectively, and g is the acceleration due to gravity. If length, time, velocity, flux and pressure are respectively non-dimensionalized with respect to a, Ω^{-1}, $a\Omega$, $a^2\Omega$ and $\rho a^2\Omega^2$, the equations of motion introduce four non-dimensional parameters; three of these are the Weber, Reynolds and Galileo numbers, respectively corresponding to capillarity, inertia and gravity, and given by

$$We = \frac{\rho a^3 \Omega^2}{\sigma}, \quad Re = \frac{a^2 \Omega \rho}{\mu} \quad \text{and} \quad Ga = \frac{g}{a\Omega^2}. \tag{2.1a–c}$$

Using these, we define (cf. Hinch & Kelmanson 2003) parameters

$$\alpha_0 \equiv \frac{Re}{We} = \frac{1}{Ca} \quad \text{and} \quad \gamma_0 \equiv Re\, Ga = St, \tag{2.2a,b}$$

in which Ca and St are respectively the capillary and Stokes numbers. A fourth non-dimensional parameter, denoted by ϵ, is defined using a characteristic dimensional film height $\bar{h}$ (defined in (2.6)) with

$$0 < \epsilon \equiv \frac{\bar{h}}{a} \ll 1. \tag{2.3}$$

Any asymptotic analysis will be valid in only a limited region of parameter space: for example, the asymptotics that capture the smooth flows in Hinch & Kelmanson (2003) require fundamental *ab initio* modification in Hinch *et al.* (2004) to accommodate shock formation as α_0 is reduced. Hence scalings must be fixed *a priori* in terms of prespecified physical parameters. Peterson, Jimack & Kelmanson (2001) and Hinch &

https://doi.org/10.1017/jfm.2014.432 Published online by Cambridge University Press

Kelmanson (2003) respectively undertake computational and asymptotic investigations of non-inertial coating flows using parameters $\alpha_0 = 10.0$, $\gamma_0 = 12.5$ and $\epsilon = 0.11298$, for which both $\epsilon\,\alpha_0$ and $\epsilon\,\gamma_0$ are strictly of order $O(1)$.

From (2.1) and (2.2), specification of α_0 and γ_0 fixes a and Ω, and hence the Reynolds number, as

$$a = \left(\frac{\gamma_0\,\sigma}{\alpha_0\,\rho\,g}\right)^{1/2}, \quad \Omega = \left(\frac{\rho\,g\,\sigma}{\gamma_0\,\alpha_0\,\mu^2}\right)^{1/2} \quad \text{and} \quad Re = \left(\frac{\gamma_0\,\sigma^3\,\rho}{\alpha_0^3\,g\,\mu^4}\right)^{1/2}. \tag{2.4a–c}$$

With the numerical values of α_0, γ_0 and ϵ given above, (2.4) reveals that $Re \approx O(\epsilon^{-1})$ for silicone oil DMS-10 at 288 K (see Hinch *et al.* (2004, p. 2990) for data source reference). Accordingly, ϵRe may be justifiably assumed to be strictly of order $O(1)$. Thus non-dimensional capillary, inertial and gravitation parameters respectively defined as

$$\alpha = \epsilon\,\alpha_0, \quad \beta' = \epsilon Re \quad \text{and} \quad \gamma = \epsilon\,\gamma_0, \tag{2.5a–c}$$

are all strictly, and physically consistently, of order $O(1)$.

The characteristic film height $\bar{h}$ introduced in (2.3) is computed from the dimensional film height $h(\theta, t)$ via

$$\bar{h} \equiv \frac{1}{2\pi}\int_0^{2\pi}\left\{h(\theta,t) + \frac{1}{2a}h(\theta,t)^2\right\}\mathrm{d}\theta, \tag{2.6}$$

because this definition, based upon mass conservation, not only ensures that ϵ is constant, but also that it is independent of fluid properties and geometric parameters; as such, $\bar{h}$ is computed using the initial profile by setting $t = 0$ in (2.6).

Introducing the intermediate variable $\hat{h}$ in the non-dimensionalization and the rescaling $h = a\,\epsilon\,\hat{h}$, the non-dimensional rescaled film thickness $\eta(\theta, t)$ defined via

$$\eta \equiv \hat{h} + \tfrac{1}{2}\epsilon\hat{h}^2 \tag{2.7}$$

is strictly of order $O(1)$, and it satisfies the one-dimensional, nonlinear, spatio-temporal evolution equation

$$\frac{\partial\eta}{\partial t} + \frac{\partial\eta}{\partial\theta} + \frac{1}{3}\frac{\partial}{\partial\theta}\left\{-\epsilon\,\gamma\,\eta^3\cos\theta - \epsilon^2\,\gamma\,\eta^3\frac{\partial\eta}{\partial\theta}\sin\theta + \epsilon^2\,\alpha\,\eta^3\frac{\partial}{\partial\theta}\left(\frac{\partial^2\eta}{\partial\theta^2} + \eta\right)\right.$$
$$\left. + \epsilon^2\,\beta'\,\eta^3\frac{\partial\eta}{\partial\theta} - \frac{2}{5}\epsilon^2\,\beta'\gamma\,\eta^5\sin\theta\right\} = 0, \tag{2.8}$$

in which the non-dimensional parameters α, β' and γ are all strictly of order $O(1)$, so that the relative interplay between capillary, gravitational and inertial effects is dictated by the residual unabsorbed powers of the small parameter ϵ in (2.8).

Further discussion is facilitated by labelling terms in (2.8) as follows,

$$\frac{\partial\eta}{\partial t} + \frac{\partial\eta}{\partial\theta} + \frac{1}{3}\frac{\partial}{\partial\theta}\left\{-\sigma_1\epsilon\,\gamma\,\eta^3\cos\theta - \sigma_2\epsilon^2\,\gamma\,\eta^3\frac{\partial\eta}{\partial\theta}\sin\theta + \sigma_3\epsilon^2\,\alpha\,\eta^3\frac{\partial}{\partial\theta}\left(\frac{\partial^2\eta}{\partial\theta^2} + \eta\right)\right.$$
$$\left. + \sigma_4\epsilon^2\,\beta'\,\eta^3\frac{\partial\eta}{\partial\theta} - \sigma_5\frac{2}{5}\epsilon^2\,\beta'\gamma\,\eta^5\sin\theta\right\} = 0, \tag{2.9}$$

https://doi.org/10.1017/jfm.2014.432 Published online by Cambridge University Press

in which each σ_i is a binary flag (i.e. $\sigma_i = 0$ or 1) that multiplies a term corresponding to a distinct physical effect, namely: σ_1 – first-order gravity; σ_2 – second-order gravity (hydrostatic pressure); σ_3 – second-order capillary; σ_4 – second-order pure-inertial; σ_5 – second-order mixed-gravitational–inertial. Hence, under this scaling, viscous entrainment is the only leading-order effect. Terms corresponding to $\sigma_{1,2,3}$ are explicitly identified as thus in the differently scaled evolution equation of Ashmore *et al.* (2003, equation (2.13)). By labelling all terms *ab initio* in the derivation of the evolution equation, it can be shown that the sources of the two different inertial terms flagged by σ_4 and σ_5 in (2.9) are respectively the radial and tangential components of the polar form of the Navier–Stokes equations.

If an evolution equation is now assigned a Boolean signature $\Sigma \equiv \sigma_1\sigma_2\sigma_3\sigma_4\sigma_5$, the scaling-dependent promotion and demotion of inertial terms discovered in Kelmanson (2009*b*) dictates the distribution of the binary flags σ_i. For example, (3.14) in Pukhnachev (1977) has signature $\Sigma = 10100$, (2.13) in Ashmore *et al.* (2003) has signature $\Sigma = 11100$, (2.36) in Kelmanson (2009*b*) has signature $\Sigma = 10110$, and (2.8) has signature $\Sigma = 11111$.

2.2. *Motivation: cyclic solutions*

In Kelmanson (2009*b*), two-timescale asymptotics are applied to (2.9) with signature $\Sigma = 10110$ to obtain a critical Reynolds number Re_c above which the asymptotic theory predicts unbounded exponentially growing solutions $\eta(\theta, t)$. However, using the spectrally accurate numerical method of Groh & Kelmanson (2009, 2012), bounded cyclic solutions of (2.9) are discovered for $Re > Re_c$; these are now discussed.

Figure 1(*a–c*) shows the spectral numerical solution of (2.9), with $\Sigma = 10110$ and $\theta = 0$, for parameters $\alpha_0 = 10.0$, $\gamma_0 = 12.5$, $\epsilon = 0.11298$ and $Re = 4.0$. This Reynolds number exceeds the critical value $Re_c \approx 2.4911$ computed in (5.7), yet the solution evidently remains periodic and bounded for large integration times. This is confirmed in figure 1(*d*), which shows the amplitude of oscillations at the arbitrary station $\theta = 0$: although the difference between consecutive maxima $\hat{\eta}(0, t)$ and minima $\check{\eta}(0, t)$ first increases, the amplitude in the time interval $t \in [0, 5000]$ asymptotes to a constant value. That is, spectrally accurate integrations of (2.9) find new cyclic solutions that are neither unstable nor asymptotically stable, as predicted by all previous studies. The analysis of this transient flow régime constitutes the remainder of this paper.

3. Inertial destabilization

3.1. *Inertial perturbation of the steady state*

The steady-state equation corresponding to (2.9) is

$$\eta + \frac{1}{3}\left\{-\sigma_1\epsilon\,\gamma\,\eta^3\cos\theta - \sigma_2\epsilon^2\,\gamma\,\eta^3\frac{\partial\eta}{\partial\theta}\sin\theta + \sigma_3\epsilon^2\,\alpha\,\eta^3\frac{\partial}{\partial\theta}\left(\frac{\partial^2\eta}{\partial\theta^2}+\eta\right)\right.$$
$$\left. + \sigma_4\epsilon^2\,\beta'\,\eta^3\frac{\partial\eta}{\partial\theta} - \sigma_5\frac{2}{5}\epsilon^2\,\beta'\gamma\,\eta^5\sin\theta\right\} = q, \tag{3.1}$$

in which the flux q is a constant. An asymptotic solution of (3.1) is sought in the form

$$\eta_s(\theta) = 1 + \sum_{k=1}^{n}\epsilon^k\eta_k(\theta) \quad \text{and} \quad q = 1 + \sum_{k=1}^{n}\epsilon^k q_k, \tag{3.2a,b}$$

https://doi.org/10.1017/jfm.2014.432 Published online by Cambridge University Press

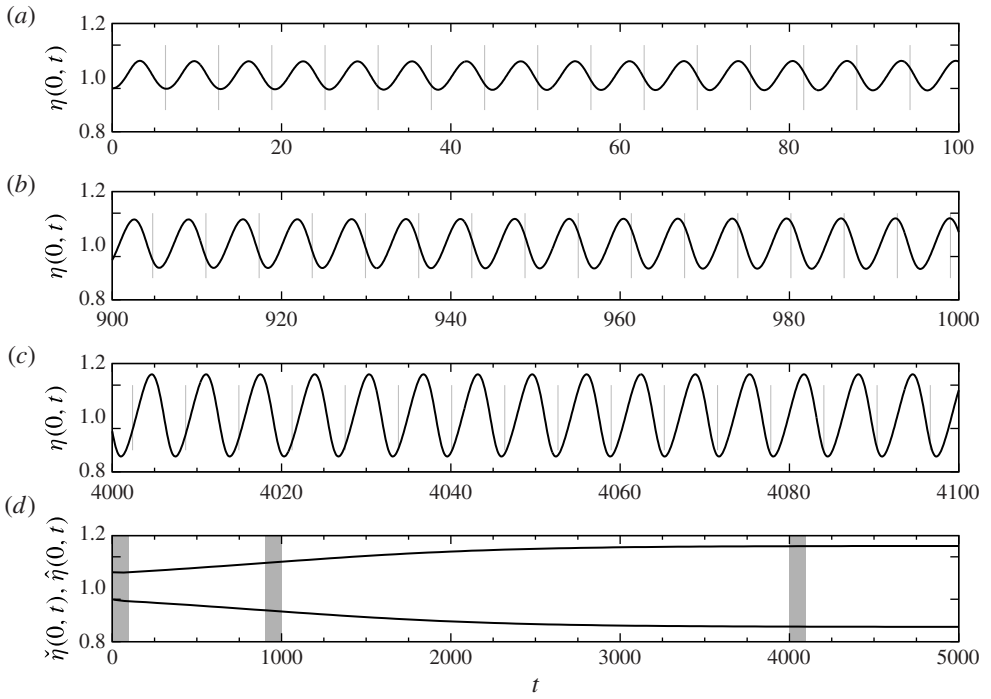


FIGURE 1. (*a*)–(*c*) Numerical solution of inertial equation (2.9) for $\Sigma = 10110$ using parameters $\alpha_0 = 10.0$, $\gamma_0 = 12.5$, $Re = 4.0$ and $\epsilon = 0.11298$ at the station $\theta = 0$. The faint vertical bars correspond to times $t = 2n\pi$ ($n \in \mathbb{N}$) at which the station $\theta = 0$ on the solid cylinder returns to its original position. The monotonically increasing separation between successive minima and the bars illustrates the cumulative gravitationally induced drift, of the free surface relative to the cylinder, resulting from the phase perturbation (4.17). (*d*) The upper and lower envelopes, respectively $\hat{\eta}$ and $\check{\eta}$, over the time integration range $t \in [0, 5000]$, superposed by shaded regions indicating the time intervals of figures (*a*–*c*). Clearly $\hat{\eta}(0, t) - \check{\eta}(0, t) \not\to 0$ as $t \to \infty$, suggesting the absence of a stable steady state, yet the divergent large-time solutions predicted by previous asymptotic analyses are not encountered.

in which the unknown coefficients η_k and q_k are readily determined by an automated process; the first three are small enough to present explicitly and are

$$\eta_1(\theta) = \tfrac{1}{3}\sigma_1\gamma\cos\theta, \tag{3.3}$$

$$\eta_2(\theta) = \tfrac{1}{6}\sigma_1^2\gamma^2\cos 2\theta \tag{3.4}$$

and

$$\eta_3(\theta) = \tfrac{1}{6}\sigma_1^3\gamma^3\cos\theta + \tfrac{1}{18}\sigma_1\sigma_2\gamma^2\cos 2\theta + \tfrac{1}{9}\sigma_1^3\gamma^3\cos 3\theta + \tfrac{1}{9}\sigma_1\sigma_4\gamma\beta'\sin\theta + \tfrac{8}{45}\sigma_1\sigma_5\gamma^2\beta'\sin 2\theta. \tag{3.5}$$

The binary flags σ_i facilitate identification of the interplay between different physical mechanisms in the formation of the steady-profile components η_k. It can be seen that η_1 arises through first-order gravity acting on the fundamental wave mode of the steady profile, η_2 through gravitational self-excitation of the fundamental mode

https://doi.org/10.1017/jfm.2014.432 Published online by Cambridge University Press

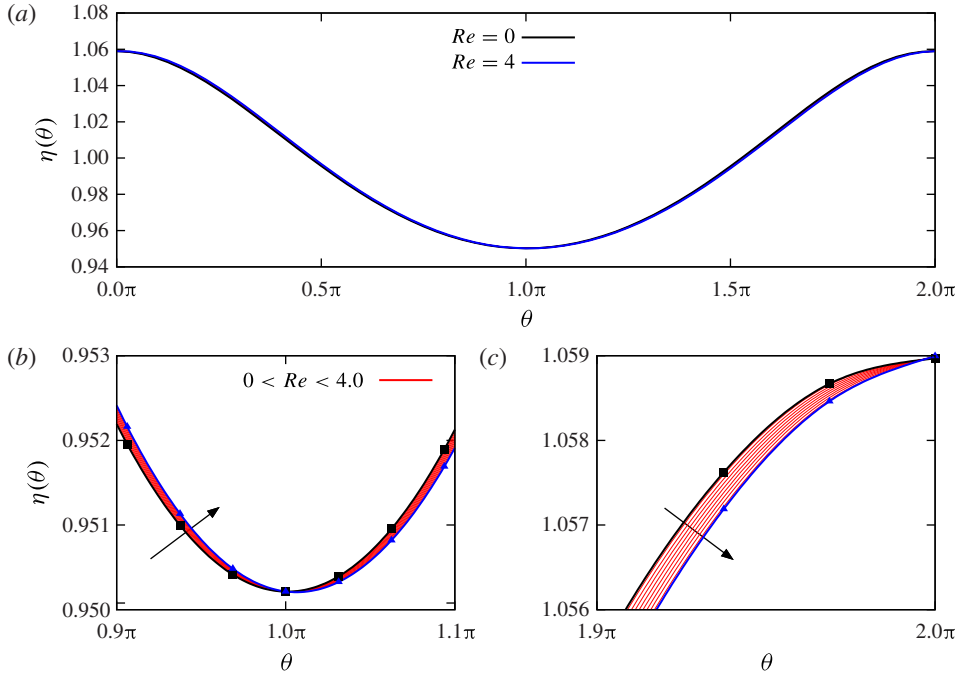


FIGURE 2. (Colour online) Spectrally accurate numerical steady-state solutions of (3.1) for Reynolds numbers increasing (in the direction of the arrows) from $Re = 0.0$ to $Re = 4.0$ in increments of 0.5, obtained with $N = 64$ collocation points and parameter values of $\alpha_0 = 10.0$, $\gamma_0 = 12.5$ and $\epsilon = 0.11298$. The discrepancy between the solutions for $Re = 0.0$ and $Re = 4.0$ is barely visible on the scale presented in (*a*), and becomes visible only when zooming in around (*b*) the minimum at $\theta \approx \pi$, and (*c*) the maximum at $\theta \approx 2\pi$. Inertia respectively raises and lowers the surface height in the ranges $[0, \pi]$ and $[\pi, 2\pi]$.

(cf. Hinch & Kelmanson 2003), and η_3 through a second gravitational self-excitation of the fundamental mode compounded by the interaction between first-order gravity and hydrostatic pressure. Hence, under the present scaling, the steady-state profile responds predominantly to gravitational effects, and is only weakly dependent upon capillarity and inertia (cf. Hansen & Kelmanson 1994), as demonstrated by the computed inertial variations presented in figure 2.

It is this inertial deformation that renders the steady-state solution unstable for sufficiently large β', as quantified in, e.g. Kelmanson (2009*b*). Inertia first appears in the asymptotic steady-state solution (3.2) in η_3, in which (3.5) reveals that β' is a positive coefficient of $\sin\theta$. Thus inertia is predicted to increase the film height in the ranges $[0, \pi]$, i.e. above the cylinder, and to decrease it in the range $[\pi, 2\pi]$, i.e. below the cylinder: these predictions are confirmed by the numerical results depicted in figure 2. Inertia therefore lifts the thin-film profile, thereby raising the centre of mass of the fluid vertically (by the appropriate symmetry of $\sin\theta$) above the centre of the cylinder; this configuration is physically analogous to the unstable equilibrium of an upright mass pendulum on a metal rod. Although the analogy provides a new heuristic physical interpretation of the cause of inertial instability, it cannot be used in isolation to quantify a critical stability threshold based on β',

https://doi.org/10.1017/jfm.2014.432 Published online by Cambridge University Press

because of the additional competing effects of gravity, capillarity and pressure on the steady-state profile. The derivation and validation of such a threshold are now undertaken.

3.2. *Linearized analysis about the steady state*

The stability of the steady state $\eta_s(\theta)$ with respect to infinitesimally small transient disturbances $\lambda(\theta,t)$ is analysed by setting $\eta(\theta,t)=\eta_s(\theta)+\lambda(\theta,t)$ in (2.9), expanding in powers of λ and linearizing to obtain the evolution equation

$$\frac{\partial\lambda}{\partial t}+\frac{\partial}{\partial\theta}\left\{A(\theta)\lambda+B(\theta)\frac{\partial}{\partial\theta}\left(\frac{\partial^2\lambda}{\partial\theta^2}+\lambda\right)+C(\theta)\frac{\partial\lambda}{\partial\theta}\right\}=0, \tag{3.6}$$

for the perturbation λ. Here,

$$\begin{aligned} A(\theta) &= 1-\sigma_1\epsilon\gamma\eta_s^2\cos\theta-\sigma_2\epsilon^2\gamma\eta_s^2\frac{\partial\eta_s}{\partial\theta}\sin\theta+\sigma_3\epsilon^2\alpha\eta_s^2\frac{\partial}{\partial\theta}\left(\frac{\partial^2\eta_s}{\partial\theta^2}+\eta_s\right), \\ &\quad +\sigma_4\epsilon^2\beta'\eta_s^2\frac{\partial\eta_s}{\partial\theta}+\frac{2}{3}\sigma_5\epsilon^2\beta'\gamma\eta_s^4\sin\theta \qquad (3.7) \\ B(\theta) &= \tfrac{1}{3}\sigma_3\epsilon^2\alpha\eta_s^3, \qquad (3.8) \\ C(\theta) &= -\tfrac{1}{3}\sigma_2\epsilon^2\gamma\eta_s^3\sin\theta+\tfrac{1}{3}\sigma_4\epsilon^2\beta'\eta_s^3, \qquad (3.9) \end{aligned}$$

in which η_s is found in § 3.1. A solution of (3.6) is sought in the form

$$\lambda=\exp(-\mathrm{i}\omega t)\phi(\theta), \tag{3.10}$$

in which the eigenvalue ω and corresponding eigenfunction ϕ are expressed as the asymptotic expansions

$$\omega=\sum_{k=0}^{n}\epsilon^k\omega_k \quad\text{and}\quad \phi(\theta)=\sum_{k=0}^{n}\epsilon^k\phi_k(\theta). \tag{3.11a,b}$$

Using (3.2) and (3.11), the decay rate $\kappa=\mathrm{Im}(\omega)$ for the fundamental mode is readily obtained via an automated procedure to have the asymptotic approximation

$$\kappa_1=\tfrac{1}{3}\sigma_4\epsilon^2\beta'-\epsilon^4\gamma^2(\sigma_1^2(3\sigma_3\alpha-\tfrac{19}{18}\sigma_4\beta')+\tfrac{2}{5}\sigma_2\sigma_5\beta')+O(\epsilon^5), \tag{3.12}$$

in which there is now revealed an ϵ^2 disparity between the leading-order influences of inertia and those of gravity and capillarity. This suggests the further inertial rescaling

$$\beta'=\epsilon^2\beta, \tag{3.13}$$

in order to establish the dominant balance that admits the fullest possible interaction between all competing physical effects for the least-stable (fundamental) mode. The revised version of (3.12) is

$$\kappa_1=\left(-3\sigma_1^2\sigma_3\alpha\gamma^2+\tfrac{1}{3}\sigma_4\beta\right)\epsilon^4+\psi_5\epsilon^5+\psi_6\epsilon^6+O(\epsilon^7), \tag{3.14}$$

where

$$\begin{aligned} \psi_5 &= \tfrac{1}{3}\sigma_1\sigma_2\sigma_3\alpha\gamma^2, \qquad (3.15) \\ \psi_6 &= -\tfrac{1}{270}\gamma^2\left(-120\sigma_2^2\sigma_3\alpha+5565\sigma_1^4\sigma_3\alpha\gamma^2-285\sigma_1^2\sigma_4\beta+108\sigma_2\sigma_5\beta\right). \qquad (3.16) \end{aligned}$$

https://doi.org/10.1017/jfm.2014.432 Published online by Cambridge University Press

By (3.14), the interplay between leading-order physical effects requires binary flags σ_1, σ_3 and σ_4 to be unity, whence the inertial parameter β enters the decay rate (3.14) with a positive sign, identifying inertia as a destabilizing effect. Hence, there exists a Reynolds number β_c above which the steady-state solution becomes unstable. With σ_2 and σ_5 still unspecified, the critical Reynolds number β_c for the fundamental mode is found to be

$$\beta_c = \frac{5\alpha\,\gamma^2\left(54 - 6\,\sigma_2\epsilon + 371\,\gamma^2\epsilon^2 - 8\,\epsilon^2\sigma_2^2\right)}{30 - 36\,\gamma^2\epsilon^2\sigma_2\sigma_5 + 95\,\gamma^2\epsilon^2} + O(\epsilon^3), \tag{3.17}$$

which, to leading order, is equivalent (upon translation of notation) to the asymptotic approximations derived via independent routes in Noakes *et al.* (2006) and Kelmanson (2009*b*). What remains unresolved is the spatio-temporal evolution of the thin film once the critical Reynolds number is exceeded; in this régime, the two-timescale asymptotics of Kelmanson (2009*b*) find an unbounded exponential growth of the free-surface instability that is, however, not corroborated by the present spectral numerical solutions shown in figure 1. The inference is that more than two timescales are required to resolve the correct form of the instability.

4. Multiple-timescale asymptotic solution

Using the multiple-timescale asymptotic method of Groh & Kelmanson (2009, 2012), new light is now shed on both the transition from stable to unstable solutions and the transient flow dynamics in the unstable régime motivated by, and discussed in, § 2.2. The evolution equation of Kelmanson (2009*b*) – which, translated into the present notation, is (2.9) with signature $\Sigma = 10110$ – is studied for two reasons. First, it allows direct comparison of results with those of the asymptotic analysis of Kelmanson (2009*b*). Second, it is the evolution equation that includes the simplest leading-order balance between all competing independent physical effects, thereby minimizing the complexity of asymptotic results in the pursuit of novel qualitative properties of the free-surface evolution. Indeed, in § 5.2 it is demonstrated beyond doubt that effects induced by the higher-order terms with factors σ_2 and σ_5 in (2.9), i.e. hydrostatic-pressure and mixed inertial–gravitational interaction respectively, are negligible by comparison with those induced by the terms present in (2.9) with signature $\Sigma = 10110$.

Equation (2.9) with signature $\Sigma = 10110$ and β rescaled by (3.13),

$$\frac{\partial\eta}{\partial t} + \frac{\partial\eta}{\partial\theta} - \frac{1}{3}\frac{\partial}{\partial\theta}\left\{\epsilon\gamma\eta^3\cos\theta - \epsilon^2\alpha\eta^3\frac{\partial}{\partial\theta}\left(\frac{\partial^2\eta}{\partial\theta^2} + \eta\right) - \epsilon^4\beta\eta^3\frac{\partial\eta}{\partial\theta}\right\} = 0, \tag{4.1}$$

is solved using the automated multiple-timescale method of Groh & Kelmanson (2009, 2012), a brief outline of which is now given. An asymptotic solution of (4.1) is sought in the form

$$\eta(\theta, t_0, \boldsymbol{t}_s) = 1 + \sum_{k=1}^{n}\epsilon^k\,\eta_k(\theta, t_0, \boldsymbol{t}_s), \tag{4.2}$$

in which $t_0 = t$ is the non-dimensional $O(1)$ timescale associated with the rotation of the cylinder, and $\boldsymbol{t}_s = (\epsilon t_0, \ldots, \epsilon^m t_0)$ is a slow-timescale m-vector. At order $O(\epsilon^k)$, the transient solution component $\eta_k(\theta, t_0, \boldsymbol{t}_s)$ in (4.2) is found to be of the form

$$\eta_k(\theta, t_0, \boldsymbol{t}_s) = \eta_k(\theta) + \sum_{j=1}^{k} f_j(\boldsymbol{t}_s)\,\cos(j\theta - jt_0 - g_j(\boldsymbol{t}_s)) + \eta_k^{(p)}(\theta, t_0, \boldsymbol{t}_s), \tag{4.3}$$

https://doi.org/10.1017/jfm.2014.432 Published online by Cambridge University Press

in which: the component $\eta_k(\theta)$ of the steady state $\eta_s(\theta)$ is defined in, e.g. (3.3)–(3.5); slow-timescale functions $f_j(\boldsymbol{t}_s)$ and $g_j(\boldsymbol{t}_s)$ respectively modulate the amplitude and drift, relative to the cylinder, of the jth wave mode of the free-surface profile; the term $\eta_k^{(p)}(\theta, t_0, \boldsymbol{t}_s)$ is a particular integral. We remark that $f_1(\boldsymbol{t}_s)$ determines the amplitude of the fundamental mode, as described in Groh & Kelmanson (2012).

For the first and higher harmonic modes, $j \geqslant 2$, amplitude-modulation functions $f_j(t)$ are found from linear secularity conditions with exponentially decaying solutions

$$f_j(t) = \exp(\kappa_j\, t), \tag{4.4}$$

in which the decay rate κ_j is

$$\kappa_j = -\tfrac{1}{3}\alpha\,\epsilon^2 j^2(j^2-1) - \tfrac{1}{9}\epsilon^4 j^2\left(\alpha\gamma^2\left(23j^2+4\right) - 3\beta\right) + O(\epsilon^6), \tag{4.5}$$

as a direct result of which

$$f_j(t) \to 0, \quad t \to \infty,\ j \geqslant 2, \tag{4.6}$$

provided that the Reynolds number is less than a critical value, $\beta < \beta_{c,j}$, at which $\kappa_j = 0$. The critical Reynolds number for higher harmonics is obtained from (4.5) as

$$\beta_{c,j} = \frac{\alpha}{\epsilon^2}\left(j^2-1\right) + \frac{1}{3}\alpha\gamma^2\left(23j^2+4\right) + O(\epsilon^2), \quad j \geqslant 2, \tag{4.7}$$

which is a quadratically increasing function of j; that is, higher modes become increasingly more stable with respect to inertial perturbations. For $\beta > \beta_{c,j}$, the asymptotic solution becomes exponentially divergent. However, (3.17) and (4.7) reveal that β_c, the critical Reynolds number for the fundamental mode, satisfies

$$\beta_c \ll \beta_{c,j}, \quad j \geqslant 2, \tag{4.8}$$

and hence the fundamental mode is more unstable than all higher harmonics; accordingly, f_1 determines the evolution of the amplitude of the thin film when (4.8) is satisfied.

The amplitude-modulation function f_1 takes the form $f_1(\epsilon^4 t) = f_1(t_4)$ because it arises in the $O(\epsilon^5)$ non-secularity condition, namely

$$\frac{\mathrm{d}f_1}{\mathrm{d}t_4} = \kappa_1 f_1 - \hat{\kappa}_1 f_1^3, \quad f_1(0) = 1, \tag{4.9a,b}$$

with solution

$$f_1(t_4) = \left\{\left(1 - \frac{\hat{\kappa}_1}{\kappa_1}\right)\exp(-2\kappa_1 t_4) + \frac{\hat{\kappa}_1}{\kappa_1}\right\}^{-1/2}, \tag{4.10}$$

in which

$$\kappa_1 = -3\alpha\gamma^2 + \frac{1}{3}\beta \quad \text{and} \quad \hat{\kappa}_1 = \frac{25}{324}\frac{\gamma^6}{\alpha}, \tag{4.11a,b}$$

and hence the parameter κ_1 in (4.10) assumes the role of a decay rate. Note that setting $\beta = 0$ in the formally derived (4.9) and (4.10) recovers the heuristically proposed 'transition equation' of Hinch *et al.* (2004, equation (5.5)) that connects smooth and shock-like solutions across disparate parameter ranges as α is reduced.

https://doi.org/10.1017/jfm.2014.432 Published online by Cambridge University Press

Augmenting κ_1 by terms arising from the analysis at orders $O(\epsilon^5)$ and $O(\epsilon^6)$, we obtain the more accurate decay rate

$$\kappa_1 = -3\alpha\gamma^2 + \tfrac{1}{3}\beta - \epsilon^2\gamma^2\left(\tfrac{371}{18}\alpha\gamma^2 - \tfrac{19}{18}\beta\right), \tag{4.12}$$

from which $\kappa_1 = 0$ yields

$$\beta_c = \alpha\gamma^2\frac{54 + 371\epsilon^2\gamma^2}{6 + 19\epsilon^2\gamma^2} \tag{4.13}$$

in agreement with (3.17) – after σ_2 and σ_5 have been set to zero – which was derived via an independent linearized stability analysis. In the case $\kappa_1 < 0$, the solution (4.10) is asymptotically stable, in the sense that $f_1(t_4) \to 0$ as $t_4 \to \infty$, in agreement with Kelmanson (2009*b*). Note that, in the rimming-flow counterpart of the present analysis, the sign of β reverses in (4.12), making the flow unconditionally unstable with respect to inertial variations, in keeping with Noakes *et al.* (2006) and Kelmanson (2009*b*).

Critical solutions of (4.1) occur when $\kappa_1 \to 0$ in (4.10); considering the limit formally reveals that

$$f_1(t_4) \to \frac{1}{\sqrt{1 + 2\hat{\kappa}_1 t_4}}, \quad \kappa_1 \to 0. \tag{4.14}$$

Hence the seven-timescale solution predicts that f_1 decays algebraically at the critical Reynolds number approximated by (3.17), in stark contrast with the non-decaying, periodic critical solutions either predicted or implied by prior studies: that is, (4.14) portends a hitherto-undiscovered flow mechanism.

By increasing inertia so that $\beta > \beta_c$, unstable solutions are obtained, but not in the unbounded sense of prior studies. Here, the algebraic-cum-exponential amplitude function f_1 in (4.10) is bounded for all values of $\kappa_1 > 0$ and has the large-time limit

$$f_1(t_4) \to \sqrt{\frac{\kappa_1}{\hat{\kappa}_1}}, \quad t_4 \to \infty, \kappa_1 > 0, \tag{4.15}$$

as a consequence of which, using (3.3), (4.3) and (4.6), and noting that $f_1(0) = 1$, the large-time profile of the film with uniform unit initial height is (after rescaling, here and subsequently, all slow timescales using $t_j = \epsilon^j t$)

$$\eta(\theta, t) \to 1 + \frac{1}{3}\gamma\epsilon\left(\cos\theta - \sqrt{\frac{\kappa_1}{\hat{\kappa}_1}}\cos\big(\theta - (1 + g_1)t\big)\right), \quad t \to \infty, \tag{4.16}$$

in which the fundamental-mode drift coefficient g_1 is determined as

$$g_1 = -\tfrac{5}{6}\gamma^2\epsilon^2 - \tfrac{25}{24}\gamma^4\epsilon^4 - \tfrac{2275}{972}\epsilon^6\gamma^6 - 12\epsilon^6\gamma^2\alpha^2 + O(\epsilon^8), \tag{4.17}$$

which is independent of the inertial parameter β to the presented order.

By (4.16), a steady-state profile cannot be attained; the flow assumes a periodic state dominated by the fundamental mode. Such (explicitly parameterized) periodic states, although having been identified numerically and experimentally, have been neither explicitly analysed nor quantified in previous asymptotic studies and so constitute a novel discovery. However, experimental and numerical evidence, which is not quantitatively analysed, of such states is respectively given in Thorodssen & Mahadevan (1997) and Hosoi & Mahadevan (1999), in which they are referred to as 'sloshing solutions'.

https://doi.org/10.1017/jfm.2014.432 Published online by Cambridge University Press

5. Results and discussion

5.1. *Qualitative validation of the asymptotic theory*

The results obtained from the asymptotics of § 4 are first corroborated on a qualitative physical basis and then quantitatively validated against the spectrally accurate numerics of Groh & Kelmanson (2009, 2012). The three-term asymptotic solution obtained using seven timescales and $\Sigma = 10110$ in (4.2) is

$$\eta(\theta, t) = 1 + \epsilon\, \eta_1(\theta, t) + \epsilon^2\, \eta_2(\theta, t) + O(\epsilon^3), \tag{5.1}$$

in which

$$\eta_1(\theta, t) = \tfrac{1}{3}\gamma \cos\theta - \tfrac{1}{3}\gamma f_1(t) \cos(\theta - t - g_1 t) \tag{5.2}$$

and

$$\eta_2(\theta, t) = \frac{1}{6}\gamma^2 \cos 2\theta - \frac{1}{3}\gamma^2 f_1(t) \cos(2\theta - t - g_1 t) - \frac{5}{108}\frac{\gamma^4}{\alpha} f_1(t)^2 \cos(2\theta - 2t - g_1 t), \tag{5.3}$$

wherein $f_1(t)$ and g_1 are given by (4.10) and (4.17) respectively. Previous asymptotic studies have used only two timescales, which is tantamount to setting $\hat{\kappa}_1 = 0$ in (4.10); in this case, the algebraic-cum-exponential amplitude $f_1(t)$ has the pure-exponential limit

$$f_1^*(t) \equiv \lim_{\hat{\kappa}_1 \to 0} f_1(t) = \exp(\kappa_1 \epsilon^4 t), \tag{5.4}$$

which fully explains all observations based on the two-timescale asymptotics of Kelmanson (2009*b*). Asymptotic solutions (5.1) using both f_1 and f_1^* can now be compared. Since our interest is in inertial perturbations of amplitude, and because inertial effects are absent from g_1 in (4.17) to the presented order, the same slowly varying phase-drift coefficient g_1 is used in both cases. The comparison is depicted in figure 3, in which inertia exceeds the predicted critical value (3.17). Both f_1 and f_1^* are seen to be in good agreement at early times, but they diverge at $t = O(400)$; the exponentially divergent solution incorporating f_1^* results in the free surface penetrating the cylinder surface at times $t = O(10^3)$, when the two-timescale results are no longer physically viable. Most strikingly, the qualitative behaviour of the solutions of (5.1) incorporating f_1 is entirely consistent with that of the 'motivating' solutions in figure 1(*a–c*), which were computed using independent spectrally accurate numerics. That is, the advanced multiple-timescale procedure has identified and explained a new physical mechanism, one that has remained beyond the reach of all previous related studies. A quantitative validation of the new asymptotic results is now conducted using the authors' spectrally accurate numerical method (Groh & Kelmanson 2009, 2012).

5.2. *Quantitative validation of the asymptotic theory*

Quantification of the asymptotic results is effected with reference to the motivating computations shown in figure 1(*d*), which shows the loci $\hat{\eta}(0, t)$ and $\check{\eta}(0, t)$ that interpolate respectively the maxima and minima of $\eta(0, t)$ in figure 1(*a–c*). It follows from (3.2), (3.3), (4.17) and (5.1) that

$$\eta(\theta, t) = \eta_s(\theta) - \tfrac{1}{3}\epsilon\gamma f_1(t) \cos(\theta - t) + O(\epsilon^2), \tag{5.5}$$

and hence that

$$\hat{\eta}(0, t) - \eta_s(0) \approx \tfrac{1}{3}\epsilon\gamma f_1(t), \tag{5.6}$$

https://doi.org/10.1017/jfm.2014.432 Published online by Cambridge University Press

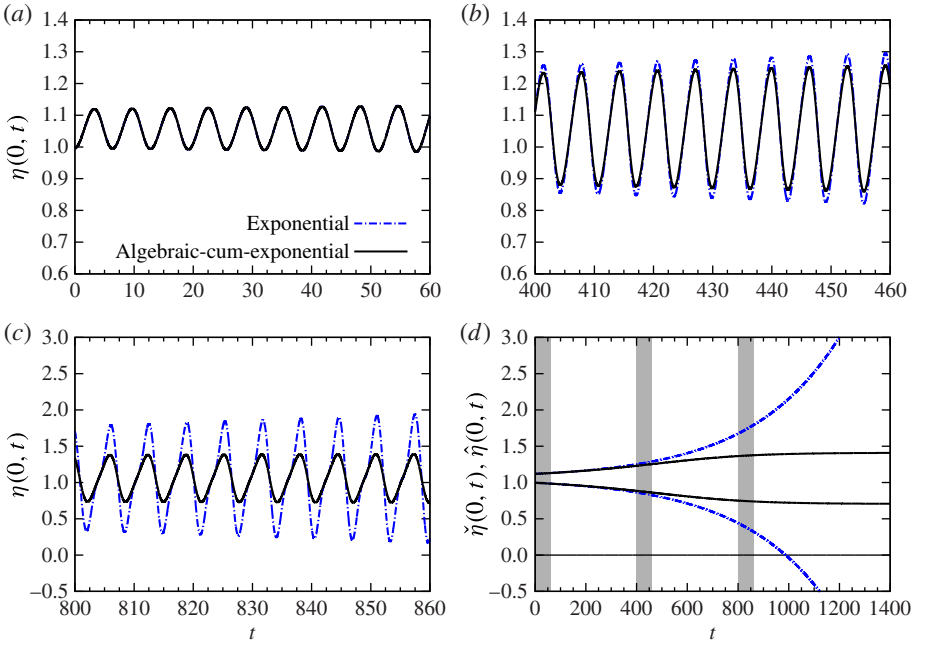


FIGURE 3. (Colour online) (*a–c*) Comparison of three-term asymptotic solutions $\eta(0,t)$ computed using f_1^* (dashed line, with exponential amplitude) and f_1 (solid line, with exponential-cum-algebraic amplitude) in (5.1). Here, $\Sigma = 10110$, and the physical parameters are $\alpha_0 = 10.0$, $\epsilon = 0.11298$, $\gamma_0 = 12.5$ and $Re = 4.0$, which value of Re exceeds the theoretical critical value Re_c predicted in (5.7). (*d*) The upper and lower envelopes, respectively $\hat{\eta}$ and $\check{\eta}$, over the time integration range $t \in [0, 1400]$, superposed by shaded regions indicating the time intervals of figures (*a–c*). Note the different vertical scales in (*a,b*) and (*c,d*). The solid curve should be qualitatively compared with the motivating numerical solutions, computed using the same parameters, shown in figure 1(*a–c*).

the right-hand (theoretical) and left-hand (numerical) sides of which can be compared. Before doing so, it is useful to make theoretical predictions and computational estimates of the critical Reynolds number Re_c at which the growth rate κ_1 of the fundamental mode vanishes. By (4.12) and the scalings (2.5) and (3.13), $\kappa_1 = 0$ when Re assumes the critical value

$$Re_c \equiv \epsilon\alpha\gamma^2 \frac{54 + 371\epsilon^2\gamma^2}{6 + 19\epsilon^2\gamma^2} \approx 2.49115 \tag{5.7}$$

when parameters $\alpha_0 = 10.0$, $\gamma_0 = 12.5$ and $\epsilon = 0.11298$ are used. The corresponding critical Reynolds number determined by the leading-order two-timescale asymptotics of Kelmanson (2009*b*, equation (4.7)) is, translated into the present notation,

$$\overline{Re}_c = \frac{9\epsilon\alpha\gamma^2}{1 + 16\epsilon^2\alpha^4} \approx 2.28363, \tag{5.8}$$

which is comparable with the value $Re_c^* \approx 2.29123$ obtained by omitting the order $O(\epsilon^2)$ terms (due to the third and higher timescales) in the rational fraction in (5.7).

https://doi.org/10.1017/jfm.2014.432 Published online by Cambridge University Press

For comparison, a computational search using the spectrally accurate numerics of Groh & Kelmanson (2009, 2012) yields a 'true' critical value of

$$\widehat{Re}_c \approx 2.49661, \tag{5.9}$$

relative to which the asymptotic prediction Re_c of (5.7) is in error by 0.2 %. The terms in (5.6) are now compared over a range of Reynolds numbers guided by (5.7)–(5.9), and chosen to highlight distinctive solution behaviour; specifically, $Re = Re_c \pm 0.01 \times 2^k$ for $k = 0, \ldots, 7$, in which the plus and minus signs respectively yield unstable and stable solutions. Theoretically and numerically determined inertial influences on stability are respectively presented in figure 4(*a,b*), which provide convincing quantitative validation of prediction (5.6). Figure 4(*a,b*) also reveal that the agreement between theory and numerics continues over large timescales as a result of the correct amplitude of the fundamental mode being fully captured by the asymptotic solution. Hence the only discrepancy (which decreases over time) between the numerical and asymptotic solutions is the one induced by the asymptotics not fully capturing the drift; such a discrepancy is not evident in the amplitude plots of figure 4. It is, moreover, the inclusion of seven timescales that underlies the above-mentioned close agreement between the theoretical Re_c of (5.7) and the 'true' numerical $\widehat{Re}_c$ of (5.9): by using only two timescales, the prediction $\overline{Re}_c$ of (5.8) underestimates the value of $\widehat{Re}_c$ by approximately 8.5 %.

In figure 4(*a*) and (*b*), the solid (blue online) and dashed (red online) curves correspond respectively to stable and unstable solutions, and the two stability régimes are divided by the solid (black) line enumerated ③. The dotted lines in figure 4(*b*) correspond to a numerical search used to obtain the curve labelled ④, at $Re = \widehat{Re}_c$ given by (5.9). The sensitivity of the stability behaviour with respect to the Reynolds number is evidenced by noting that the curves labelled ③ and ④ in figure 4(*b*) are computed using values of Re that differ (see above) by only 0.2 % in a relative sense. Also apparent in figure 4(*a,b*) is that unstable solutions not only remain bounded (whilst remaining constant over large timescales, cf. figure 1(*d*)), but also that they have an amplitude that increases with Re; the functional dependence of the amplitude upon Re is determined in § 5.3. Note, for comparison, that the equivalent of figure 4(*a*) for the two-timescale asymptotics of Kelmanson (2009*b*) would contain curves for $Re > Re_c$ (dashed lines) that diverge exponentially in the manner of $\hat{\eta}$ (the upper envelope) in figure 3(*d*).

The theoretical average decay rate $\langle\kappa\rangle$ of all instantaneous decay rates $\kappa(t)$ over the time interval $t \in [0, T]$ is obtained from (4.10) as

$$\langle\kappa\rangle \equiv \frac{1}{T}\int_0^T \frac{\mathrm{d}}{\mathrm{d}\tau}\ln f(\tau)\,\mathrm{d}\tau = -\frac{1}{2T}\ln\left\{\left(1-\frac{\hat{\kappa}_1}{\kappa_1}\right)\exp(-2\kappa_1\epsilon^4 T) + \frac{\hat{\kappa}_1}{\kappa_1}\right\}. \tag{5.10}$$

By using Lagrange polynomials to interpolate the numerical solution $\eta(\theta, t)$ over successive cycles, consecutive extrema of $\eta(\theta, t)$ at some fixed station (here, $\theta = 0$) can be accurately approximated and post-processed to compute a numerical average decay rate $\langle\hat{\kappa}\rangle$ from the envelopes of the extrema. The comparison between $\langle\kappa\rangle$ and $\langle\hat{\kappa}\rangle$ is conducted in figure 5, in which both decay rates are further compared with the (pure-exponential) decay rate determined by the two-timescale asymptotics of Kelmanson (2009*b*). It is evident that the two-timescale decay rate is a reasonable qualitative approximation in the stable régime, whereas the seven-timescale result provides both a qualitatively and quantitatively good estimate of the averaged

https://doi.org/10.1017/jfm.2014.432 Published online by Cambridge University Press

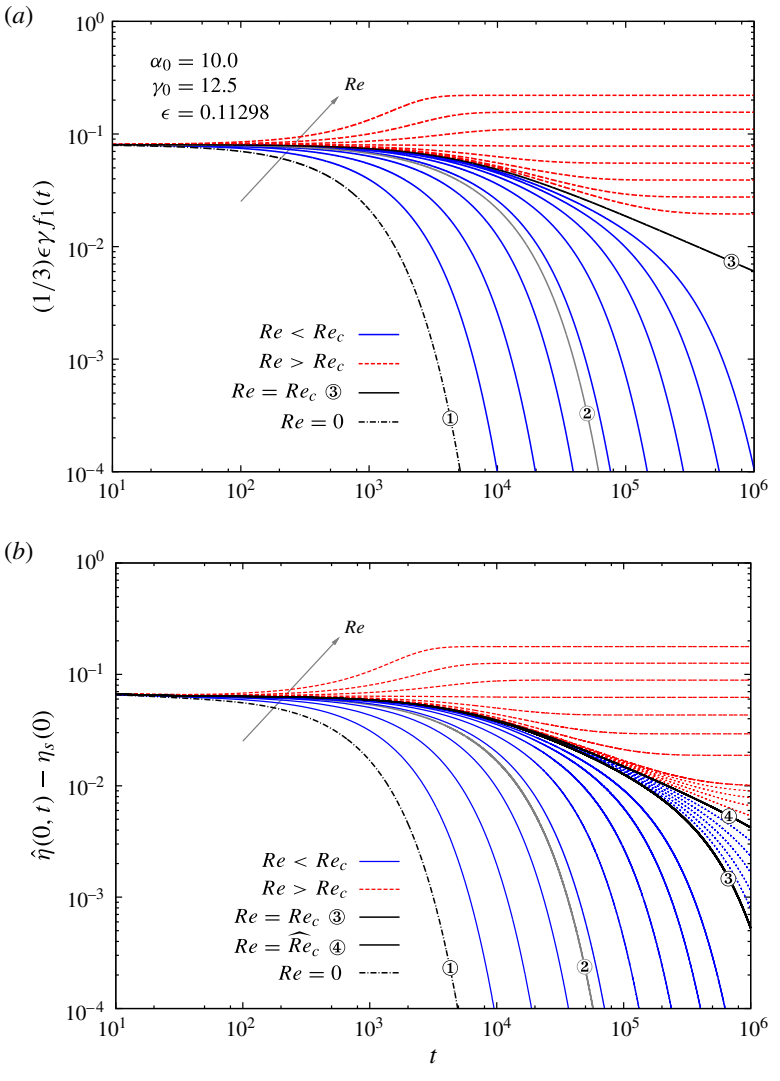


FIGURE 4. (Colour online) Quantitative validation of prediction (5.6): the theoretical values (*a*) of $(1/3)\epsilon\gamma f_1(t)$ are in excellent quantitative agreement with the corresponding numerical values (*b*) of $\hat{\eta}(0,t) - \eta_s(0)$ over the integration range $t \in [0, 10^6]$. Here, $\Sigma = 10110$, $\alpha_0 = 10.0$, $\gamma_0 = 12.5$ and $\epsilon = 0.11298$. The curve enumerated ① corresponds to the solution with $Re = 0$. Remaining enumerated curves are critical solutions with: ② $Re = \overline{Re}_c$ given by (5.8); ③ $Re = Re_c$ given by (5.7); ④ $Re = \widehat{Re}_c$ given by (5.9). Solid curves (blue online) correspond to stable solutions obtained for $Re = Re_c - 0.01 \times 2^k$, and dashed curves (red online) correspond to unstable solutions obtained for $Re = Re_c + 0.01 \times 2^k$, for $k = 1, \ldots, 7$. Arrows point in the direction of increasing Re, and the dotted lines in (*b*) are obtained from a numerical search for the 'true' critical Reynolds number $Re = \widehat{Re}_c$. The sensitivity of results to variations in Re is quantified by noting that $\Delta Re = 5.46 \times 10^{-3}$ separates the curves labelled ③ and ④ in (*b*); hence the agreement between results in (*a*) and (*b*) quantifies the impressive accuracy of the seven-timescale asymptotics.

https://doi.org/10.1017/jfm.2014.432 Published online by Cambridge University Press

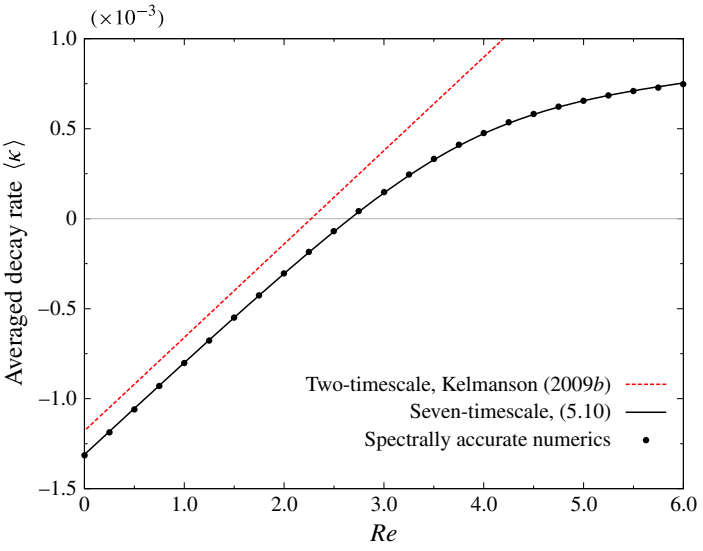


FIGURE 5. (Colour online) The numerical and asymptotic average decay-rate dependence on the Reynolds number Re for $\Sigma = 10110$, $\alpha_0 = 10.0$, $\gamma_0 = 12.5$ and $\epsilon = 0.11298$. The two-timescale asymptotics of Kelmanson (2009*b*) capture the qualitative behaviour in the stable régime $\langle\kappa\rangle < 0$. The present seven-timescale asymptotics capture both the qualitative and quantitative behaviour extremely well in both the stable and unstable régimes, as confirmed by spectrally accurate numerics. A value of $T = 10^6$ has been used in (5.10).

decay rate in both the stable and unstable régimes. The divergence from the linear dependence in the unstable régime is a result of the algebraic-cum-exponential amplitude dependence of the fundamental mode that has eluded – indeed, lies beyond the methodology of – all prior studies; it is, moreover, fully corroborated by quantifying spectral numerics.

The effect of altering the signature Σ in (2.9) is demonstrated in figure 6, which shows the changes induced in the results depicted in figure 5 when the binary flags σ_2 and σ_5, thus far set to zero, are switched on either independently or together. The figure clearly evidences that the influences of both hydrostatic pressure and gravitational–inertial interaction, although perturbing the results due to the leading-order effects of capillarity, gravity and 'pure' inertia quantitatively, do not do so qualitatively. That is, in the large-time limit, solutions are exponentially convergent to a steady-state profile in the stable régime, whereas they approach a time-dependent periodic state in the unstable régime that is stable to secondary perturbations by subservient physical effects. Consequently, the application of the seven-timescale asymptotics to the simpler evolution equation (4.1) – equivalent to Kelmanson (2009*b*, equation (2.36)) and asymptotically equivalent to a two-dimensional restriction of Noakes *et al.* (2006, equation (3.13)) – is justified.

In order to demonstrate that the seven-timescale asymptotics work well in more extended parameter régimes than those implicit in figures 5 and 6, a density plot is presented in figure 7 of numerically integrated large-time decay rates in the Re–γ_0 plane for fixed α_0 and ϵ. In figure 7, the upper-left (blue online) and lower-right (red online) regions correspond respectively to stable and unstable solutions, and

https://doi.org/10.1017/jfm.2014.432 Published online by Cambridge University Press

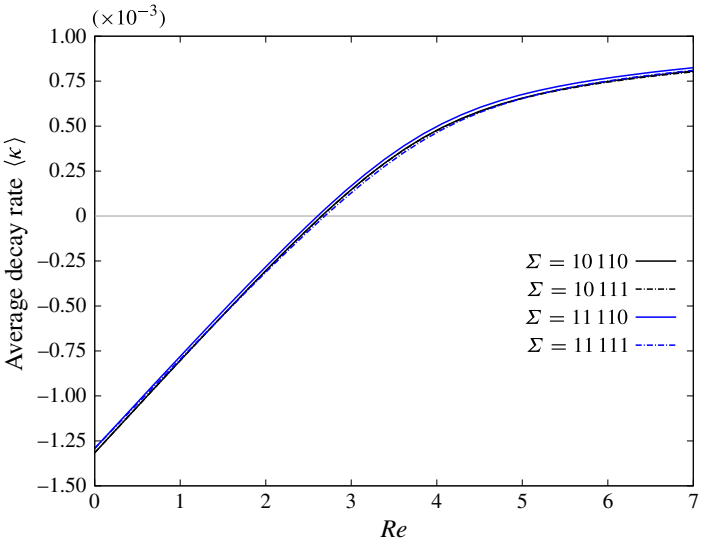


FIGURE 6. (Colour online) The asymptotically predicted decay-rate dependence on Re computed with the same physical parameters as in figure 5, but with the signatures Σ altered by switching σ_2 and σ_5 on and off. Imperceptible differences occur in the results, evidencing that the influences of hydrostatic pressure and gravitational–inertial interaction are dominated by those due to leading-order capillarity, gravity and 'pure' inertia.

the theoretically predicted critical separatrix (solid line) between the two regions is only 0.2 % in error, which is almost indistinguishable on this scale from its numerically computed counterpart (dotted line).

5.3. *Periodic state*

The secularity condition (4.9) for the fundamental-mode amplitude function f_1 becomes, upon using (5.7),

$$\frac{\mathrm{d}f_1}{\mathrm{d}t_4} = \frac{1}{3\epsilon}(Re - Re_c)f_1 - \frac{25\gamma^6}{324\alpha}f_1^3, \tag{5.11}$$

which is the canonical equation (Tu (1994, p. 198)) of a supercritical pitchfork bifurcation parameterized by $Re - Re_c$. Solutions of (5.11) are therefore asymptotically stable; they decay to zero for $Re < Re_c$ and become stable limit cycles with an amplitude proportional to $(Re - Re_c)^{1/2}$ when $Re \geqslant Re_c$. It is also noteworthy that, although five-timescale asymptotics also yield the second term on the right-hand side of (5.11), seven-timescale asymptotics are the minimum necessary to determine an f_1 whose behaviour agrees quantitatively with numerical integrations, as evidenced in figure 8 and the associated discussion. In fact, the second term on the right-hand side of (5.11) is born of the higher-harmonic 'modal interactions' discussed in § 6 and, in more detail, in Groh & Kelmanson (2012). Although experimental and numerical evidence for the existence of cyclic states is respectively given in Thorodssen & Mahadevan (1997) and Hosoi & Mahadevan (1999), the present work comprises the first combined qualitative and quantitative transient analysis of such régimes for coating (and, by implication, rimming) flows.

https://doi.org/10.1017/jfm.2014.432 Published online by Cambridge University Press

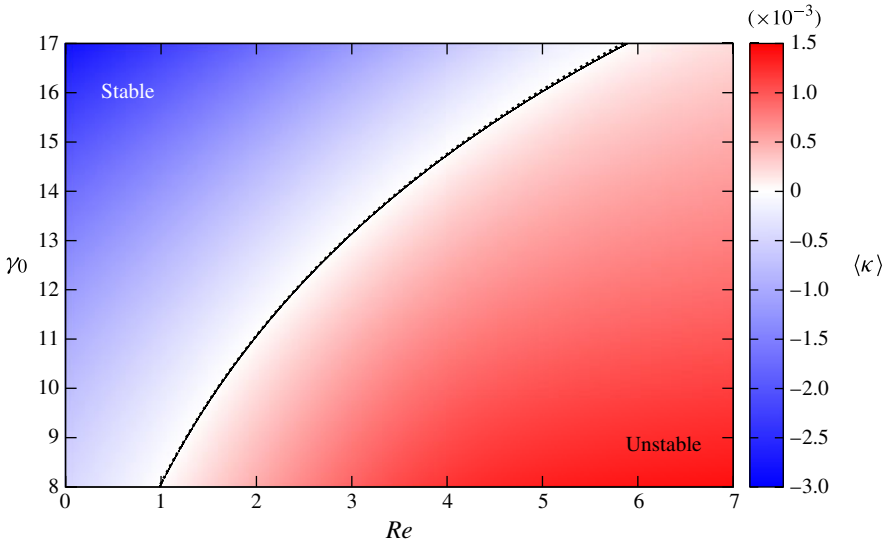


FIGURE 7. (Colour online) A density plot of the decay rate $\langle\kappa\rangle$ in Re–γ_0 space for signature $\Sigma = 10110$ and parameters $\alpha_0 = 10.0$, $\epsilon = 0.11298$ and $T = 10^6$ in (5.10). Decay rates are obtained from numerical integrations of the evolution equation: the upper-left (blue online) and lower-right (red online) regions correspond respectively to stable and unstable solutions. The dotted line is the $\langle\kappa\rangle = 0$ critical-stability separatrix computed from numerical integrations; this compares well with the solid line obtained from the theoretical result (5.7). It is not possible to predict the value of $Re \gg Re_c$ at which cyclic solutions eventually yield to inertially dominated unconditional instability. It is to be noted, however, that figures 10(*d*) and 11(*b*) evidence the existence of (spectrally accurate, computed) cyclic solutions for $Re = 60.0$, which is (still) of the order $Re \approx O(\epsilon^{-1})$ stated below (2.4); increasing this to $Re \approx O(\epsilon^{-2})$ violates the hierarchy within which the present asymptotics are developed.

By (4.16) and (4.17), the periodic component $\eta_p(\theta, t)$ of the large-time solution is given at the station $\theta = 0$ by

$$\eta_p(0, t) = -A\cos(1 + g_1)t \quad \text{for } t \gg 1, \tag{5.12}$$

in which the leading-order amplitude A is

$$A \sim \tfrac{1}{3}\epsilon\gamma F_1, \tag{5.13}$$

wherein

$$F_1 = \lim_{t\to\infty} f_1(t) = \frac{6}{5\gamma^3}\sqrt{\frac{3\alpha}{\epsilon}(Re - Re_c)} \quad \text{for } Re > Re_c, \tag{5.14}$$

in which the argument of the square root is always positive. Figure 8 shows the leading-order result (5.13) and (5.14) as a dot–dashed line: comparison with the results of spectrally accurate numerics reveals the correct qualitative amplitude growth, but a quantitative discrepancy. To reduce the discrepancy between asymptotic results and numerical computations, fundamental-mode contributions from higher-order

https://doi.org/10.1017/jfm.2014.432 Published online by Cambridge University Press

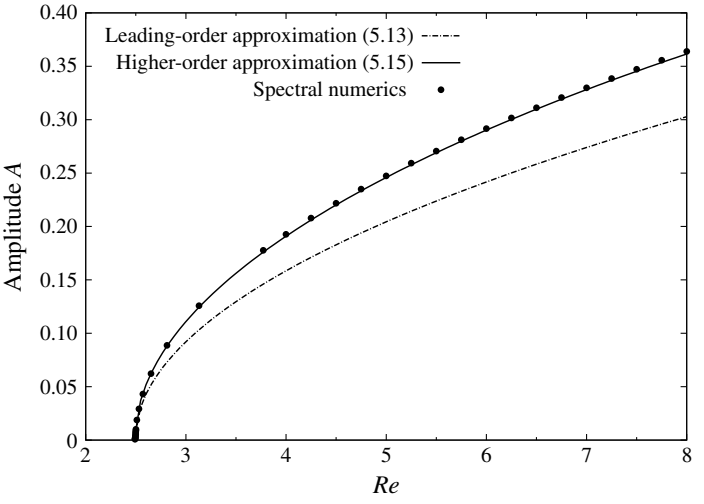


FIGURE 8. The amplitude A of the non-decaying periodic state induced by the instability of the fundamental mode as a function of the Reynolds number Re. Other parameters are as given in the caption of figure 7. The dot–dashed and solid lines respectively correspond to leading- and higher-order asymptotic approximations.

components η_k for $k \geqslant 2$ must be included in (5.13); this yields the amended amplitude estimate

$$A \sim \frac{1}{3}\epsilon\gamma F_1 \left\{1 + \gamma\epsilon + \frac{1}{3}\gamma^2\epsilon^2 \left(\left(4 - F_1 + \frac{25}{864}\frac{\gamma^4}{\alpha^2}F_1^2\right)\right)\right\} + O(\epsilon^4), \tag{5.15}$$

in which the terms of order $O(\epsilon^4)$ are known explicitly; although they are not presented because of their cumbersome nature, they are included in (5.15) when deriving the results presented in figure 8, which clearly illustrates that the higher-order amplitude dependence (5.15) is now in excellent quantitative agreement with the spectrally accurate results. Thus the parametric influence on the amplitude of the fundamental-mode component of large-time limit cycles has been explicitly determined.

Although never before explicitly analysed, periodic states have been reported in experiments: Benjamin *et al.* (1993) report that 'flows never settle into steady states' and that they 'vary periodically in time'. Moffatt (1977) reports instabilities that form 'lobes', which rotate with a speed slightly less than that of the cylinder. This is confirmed by the present theory, in which the period of the motion described by (5.12) is $2\pi/(1 + g_1)$, which is greater than the rotation period 2π of the cylinder because, by (4.17), the drift factor g_1 is always negative; hence the maximum of the periodic state lags behind the rotating cylinder, as illustrated in figures 1(*a–c*) and 9. Furthermore, the exhaustive experimental investigation of Thorodssen & Mahadevan (1997) and the numerical study of Hosoi & Mahadevan (1999) report 'sloshing solutions' and undulations, which are identified with the periodic state predicted by the present asymptotic theory. Although the periodic-state solution resembles features that are reported in experiments and numerical studies, it is acknowledged that experiments such as those conducted in Moffatt (1977) and Hynes (1978) may be influenced by three-dimensional effects that are theoretically analysed neither here nor

https://doi.org/10.1017/jfm.2014.432 Published online by Cambridge University Press

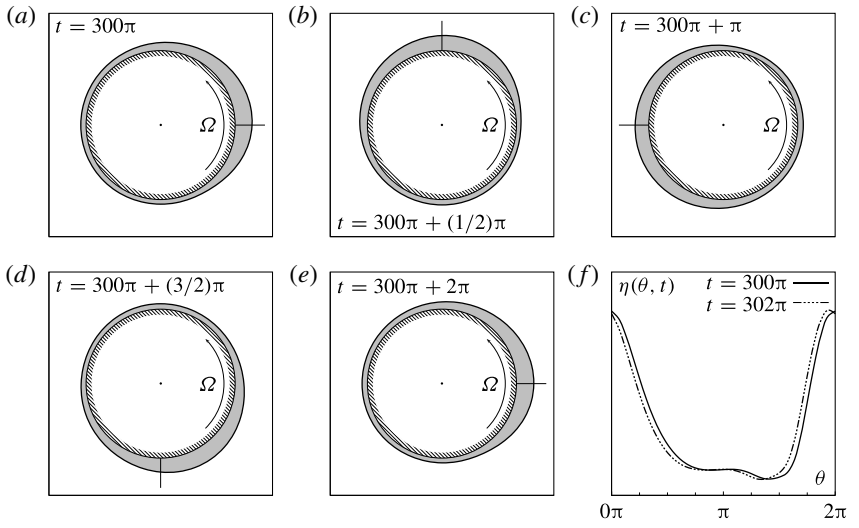


FIGURE 9. Large-time rotation of the film-thickness maximum around the cylinder, illustrated for a periodically unstable flow: the marker pin (short radial line in (*a–e*)) fixed in the free surface travels anticlockwise with the speed of the cylinder, whereas the film-thickness maximum lags, as illustrated by the cumulative single-period lag in (*f*). This phenomenon was first reported in the experiments of Moffatt (1977), where a lobe formed on a three-dimensional instability.

in the great majority of the related literature. However, it is natural to ask how the onset of instability might be affected by such axial variations, which are precluded by a two-dimensional analysis. Hosoi & Mahadevan (1999), Pougatch & Frigaard (2011) and Benilov & Lapin (2013) have considered this question by analysing three-dimensional perturbations from a two-dimensional steady state, $h_\infty(\theta)$ say, in the form $h(\theta, z, t) = h_\infty(\theta) + f(\theta)\,\exp(st + \mathrm{i}kz)$, determining eigenfunctions $f(\theta)$ and corresponding growth rates s as a function of the axial wavenumber k. Hynes (1978, equation (3.7)) appears to be the first to do this in a 3-D stability analysis that includes centrifugal, capillary and gravitational effects. Hosoi & Mahadevan (1999) find 'the existence of unstable [axial] modes only when inertia is sufficiently large'. Benilov & Lapin (2013) find that 'the strongest instability occurs for two-dimensional flows' – i.e. that axial instability does not occur before the azimuthal one. Pougatch & Frigaard (2011) conclude that 'Although we cannot say that for all flow parameters ... the 2D steady solution loses stability to a 3D solution, for at least some parameter sets this is the natural evolution'. Hence, to date, there would appear to be no comprehensive qualitative and/or quantitative resolution of the interplay between axial and azimuthal inertial effects on stability. We believe that there is no conceptual reason why the approach used in this paper cannot be extended to resolve this issue via an explicit three-dimensional asymptotic analysis.

Note that, when $Re > Re_c$, the linear term in (5.11) is positive and it can be made to dominate (in magnitude) the negative cubic term by letting $\epsilon \to 0$, in which limit f_1 apparently undergoes exponential growth. This arguably counterintuitive result is explained by noting that, in the limit $\epsilon \to 0$, the free-surface profile becomes increasingly circular, because it approaches the cylinder surface, thereby weakening the stabilizing effect of capillarity, whose role is that of annihilating first and higher

https://doi.org/10.1017/jfm.2014.432 Published online by Cambridge University Press

harmonics in the free-surface profile. That is, as the film gets thinner, it becomes less stable, but in the sense that it takes longer to approach the steady state; this observation is consistent with the results of Hinch & Kelmanson (2003), in which two-timescale asymptotics predict an exponential decay of the fundamental mode to the steady state at a rate proportional to ϵ^7.

6. Higher-mode instability

The discrepancy between leading- and higher-order results in figure 8 invites further examination of the instability of higher modes $\exp(\mathrm{i}j(\theta - t))$ (in which both $\mathrm{i} = \sqrt{-1}$ and $j \geqslant 2$ are henceforth implied), for which the seven-timescale solution of § 4 and the asymptotic analysis of Kelmanson (2009*b*) predict exponentially divergent solutions that are not corroborated by the present spectral numerics. Specifically, (4.7) predicts that the amplitude f_j of the jth mode in (4.4) increases exponentially when the Reynolds number exceeds a critical value $Re_{c,j}$ given by (4.5) as

$$Re_{c,j} \equiv \alpha_0 \left(j^2 - 1\right) + \tfrac{1}{3}\alpha_0\gamma_0^2(23j^2 + 4)\epsilon^4, \tag{6.1}$$

in which, by (4.8), $Re_{c,j} \gg Re_c$, reiterating that the fundamental mode is the least stable with respect to inertial increase. For parameters $\alpha_0 = 10.0$, $\gamma_0 = 12.5$ and $\epsilon = 0.11298$, (6.1) gives $Re_{c,2} = 38.15$ and $Re_{c,3} = 97.91$ for the second and third modes respectively; hence the solution for $Re = 60.0$ is expected to have unstable fundamental and second modes, but stable third and higher modes.

The numerical solution at the station $\theta = 0$, for $\alpha_0 = 10.0$, $\gamma_0 = 12.5$, $Re = 60.0$ and $\epsilon = 0.11298$, is shown in figure 10(*a*), in which four distinct intervals are enumerated. In interval ①, the solution is sinusoidal because of the dominant fundamental mode. At times $t = O(40)$, multi-modal interactions appear; these become increasingly more prominent in region ②, until $t = O(120)$, when further interactions arise in region ③. The solution then appears to settle into a periodic state in region ④ for times larger than $t = O(200)$.

The behaviour in intervals ①, ② and ④ can be explained by proposing a model solution (at the arbitrary station $\theta = 0$) of the form

$$\eta_m(t) = 1 + c_1 f_1(t)\ \cos t + c_2 f_2(t)\ \cos 2t, \tag{6.2}$$

in which $c_1 \gg c_2$. The functional dependence of f_1 is given in (4.10) and the amplitude function of the second mode is now proposed to behave not as (4.4) but, rather, as

$$f_2(t) = \left\{ \left(1 - \frac{\hat{\kappa}_2}{\kappa_2}\right) \exp(-2\kappa_2 t) + \frac{\hat{\kappa}_2}{\kappa_2} \right\}^{-1/2}, \tag{6.3}$$

in which κ_2 is given by (4.5) and $\hat{\kappa}_2 > 0$. Guided by (3.3), (3.4) and (4.12), the values

$$c_1 = \frac{1}{3}\gamma_0\epsilon^2, \quad c_2 = \frac{1}{6}\gamma_0^2\epsilon^4 \quad \text{and} \quad \hat{\kappa}_2 = \frac{25\gamma_0\epsilon^5}{324\alpha_0} \tag{6.4a–c}$$

are assigned to the as-yet-unspecified elements of (6.2) and (6.3) in order to effect a comparison with the numerical solution.

A comparison of figures 10(*a,b*) demonstrates that the proposed model solution $\eta_m(t)$ depicted in the latter models well the behaviour in time intervals ① and ②, i.e. the initial dominance of the fundamental mode in region ① and the onset of multi-modal

https://doi.org/10.1017/jfm.2014.432 Published online by Cambridge University Press

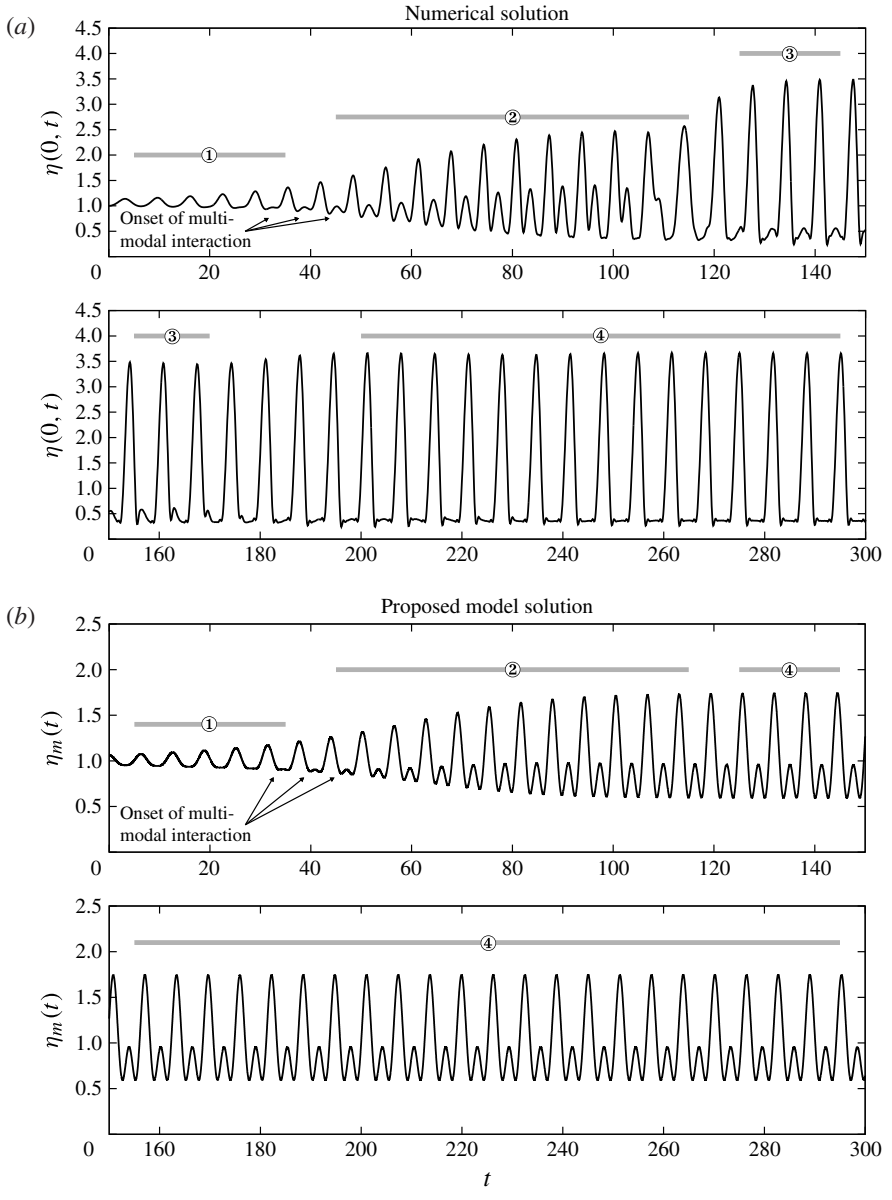


FIGURE 10. The evolution of (*a*) the numerical solution $\eta(0, t)$ and (*b*) the proposed model solution $\eta_m(t)$ given by (6.2)–(6.4). The parameters are $\alpha_0 = 10.0$, $\gamma_0 = 12.5$, $\epsilon = 0.11298$ and $Re = 60.0$, so that $Re \in (Re_{c,2}, Re_{c,3})$. The enumeration of temporal sections of the solution is discussed in the text.

interactions induced by the growth of the second mode in region ②. A periodic state is, however, attained earlier in (theoretical) figure 10(*b*) than in (numerical) figure 10(*a*) because the growth in the former of third and higher modes in region ③ is precluded by the truncated form of (6.2), whereas the numerical solution admits nonlinear interactions with modes having $j \geqslant 3$.

The agreement between the proposed model solution and the numerical results suggests that the amplitude of the higher modes must in reality also satisfy a

https://doi.org/10.1017/jfm.2014.432 Published online by Cambridge University Press

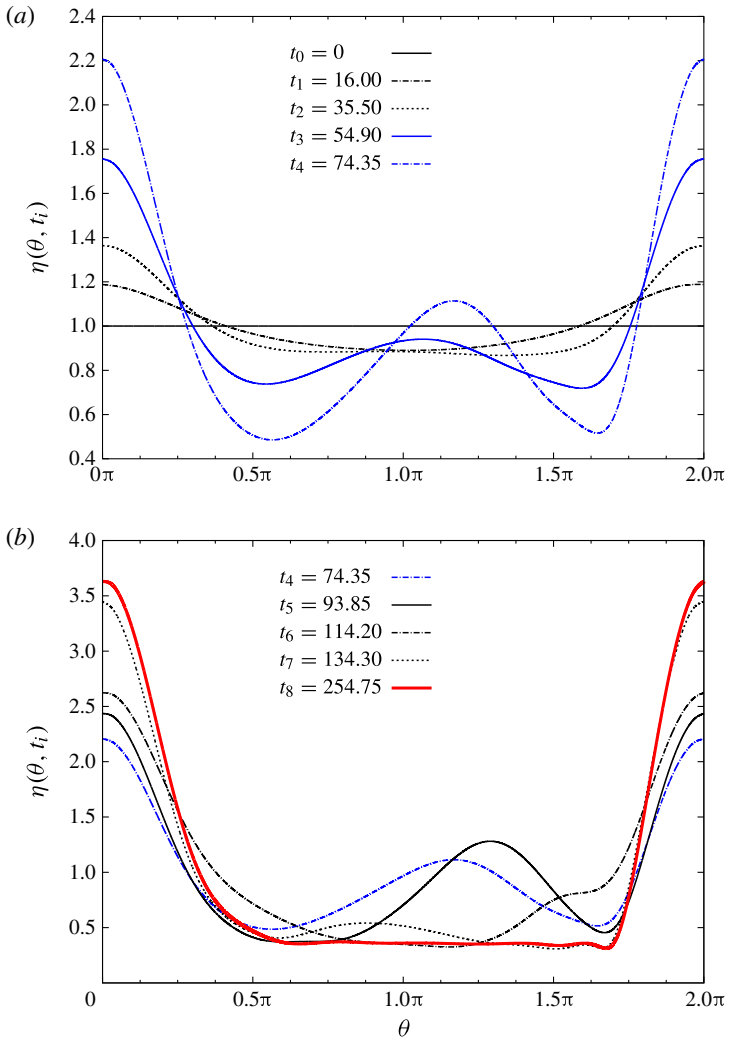


FIGURE 11. (Colour online) Evolving snapshots of the free-surface profile with parameters $\alpha_0 = 10.0$, $\gamma_0 = 12.5$, $Re = 60.0$ and $\epsilon = 0.11298$. Early and later profiles are respectively separated into plots (*a,b*) for clarity. The constant initial profile develops for $t \in [t_0, t_2]$ into a sinusoidal shape, after which a second, less-pronounced, maximum develops for $t \in [t_2, t_5]$. As the periodic state is approached for $t \in [t_6, t_8]$, the film profile converges to a near-constant solution with the exception of a single localized maximum.

differential equation of the algebraic-cum-exponential form (4.9) rather than the pure-exponential form (4.4). The implication is that (even) the seven-timescale method cannot determine the correct form of the secularity conditions for the higher modes, and an explanation of this technical methodological aspect, being beyond the remit of this paper, would merit future consideration.

Finally, presented in figure 11 is a sequence of temporal snapshots of the seven-timescale solution $\eta(\theta, t_k)$, showing the evolution of the free surface around the full cylinder. The early solution, with $k = 1$ in figure 11(*a*), is the pure-sinusoidal fundamental mode, from which higher-order modes develop and interact with

https://doi.org/10.1017/jfm.2014.432 Published online by Cambridge University Press

increasing t by the mechanisms described in Hinch & Kelmanson (2003, section 6). The late solution, with $k = 8$ in figure 11(*b*), shows a near-uniform solution outside a relatively localized region in which there is a pronounced unique maximum. Although these lobes have been predicted via a two-dimensional analysis that ignores axial effects, they are reminiscent of the cylindro-stationary lobes observed in both the experiments of Moffatt (1977) and the steady-state results of Karabut (2007) and Pougatch & Frigaard (2011).

REFERENCES

Ashmore, J., Hosoi, A. E. & Stone, H. A. 2003 The effect of surface tension on rimming flows in a partially filled rotating cylinder. *J. Fluid Mech.* **479**, 65–98.

Benilov, E. S. & Lapin, V. N. 2013 Inertial instability of flows on the inside or outside of a rotating cylinder. *J. Fluid Mech.* **736**, 107–129.

Benilov, E. S. & O'Brien, S. B. G. 2005 Inertial instability of a liquid film inside a rotating horizontal cylinder. *Phys. Fluids* **17**, 1–16.

Benjamin, T. B., Pritchard, W. G. & Tavener, S. J. 1993 Steady and unsteady flows of a highly viscous liquid inside a rotating horizontal cylinder. *Report No.* AM 122. Department of Mathematics, Penn State University.

Evans, P. L., Schwarz, L. W. & Roy, R. V. 2004 Steady and unsteady solutions for coating flow on a rotating horizontal cylinder: two-dimensional theoretical and numerical modeling. *Phys. Fluids* **16**, 2742–2756.

Evans, P. L., Schwarz, L. W. & Roy, R. V. 2005 Three-dimensional solutions for coating flow on a rotating horizontal cylinder: theory and experiment. *Phys. Fluids* **17**, 072102.

Groh, C. M. & Kelmanson, M. A. 2009 Multiple-timescale asymptotic analysis of transient coating flows. *Phys. Fluids* **21**, 091702.

Groh, C. M. & Kelmanson, M. A. 2012 Computer-algebra multiple-timescale method for spatially periodic thin-film viscous-flow problems. *Intl J. Numer. Meth. Fluids* **68**, 1457–1470.

Hansen, E. B. & Kelmanson, M. A. 1994 Steady, viscous, free-surface flow on a rotating cylinder. *J. Fluid Mech.* **272**, 91–107.

Hinch, E. J. & Kelmanson, M. A. 2003 On the decay and drift of free-surface perturbations in viscous, thin-film flow exterior to a rotating cylinder. *Proc. R. Soc. Lond.* A **459**, 1193–1213.

Hinch, E. J., Kelmanson, M. A. & Metcalfe, P. D. 2004 Shock-like free-surface perturbations in low-surface-tension, viscous, thin-film flow exterior to a rotating cylinder. *Proc. R. Soc. Lond.* A **460**, 2975–2991.

Hosoi, A. E. & Mahadevan, L. 1999 Axial instability of a free-surface front in a partially filled horizontal rotating cylinder. *Phys. Fluids* **11**, 97–106.

Hynes, T. P. 1978 The stability of thin flims. DPhil thesis, Churchill College, Cambridge.

Karabut, E. A. 2007 Two régimes of liquid film flow on a rotating cylinder. *J. Appl. Mech. Tech. Phys.* **48** (1), 55–64.

Kelmanson, M. A. 2009*a* Pseudo-three-timescale approximation of exponentially modulated free-surface waves. *J. Fluid Mech.* **625**, 435–443.

Kelmanson, M. A. 2009*b* On inertial effects in the Moffatt–Pukhnachov coating-flow problem. *J. Fluid Mech.* **633**, 327–353.

Moffatt, H. K. 1977 Behaviour of a viscous film on the outer surface of a rotating cylinder. *J. Méc.* **187**, 651–673.

Noakes, C. J., King, J. R. & Riley, D. S. 2006 On the development of rational approximations incorporating inertial effects in coating and rimming flows: a multiple-scales approach. *Q. J. Mech. Appl. Maths* **59**, 163–190.

Peterson, R. C., Jimack, P. K. & Kelmanson, M. A. 2001 On the stability of viscous free-surface flow supported by a rotating cylinder. *Proc. R. Soc. Lond.* A **457**, 1427–1445.

Pougatch, K. & Frigaard, I. 2011 Thin film flow on the inside surface of a horizontally rotating cylinder: steady state solutions and their stability. *Phys. Fluids* **23**, 022102.

https://doi.org/10.1017/jfm.2014.432 Published online by Cambridge University Press

PUKHNACHEV, V. V. 1977 Motion of a liquid film on the surface of a rotating cylinder in a gravitational field. *J. Appl. Mech. Tech. Phys.* **18**, 344–351.

THORODSSEN, S. T. & MAHADEVAN, L. 1997 Experimental study of coating flows in a partially-filled horizontal rotating cylinder. *Exp. Fluids* **23**, 1–13.

TU, P. N. V. 1994 *Dynamical Systems*, 2nd edn. Springer-Verlag.

https://doi.org/10.1017/jfm.2014.432 Published online by Cambridge University Press